Ice Water Path Estimation and Characterization Using Passive Microwave Radiometry

J. VIVEKANANDAN, J. TURK AND V. N. BRINGI

Department of Electrical Engineering, Colorado State University, Fort Collins, Colorado

(Manuscript received 6 September 1990, in final form 14 March 1991)

ABSTRACT

Microwave emission emerging from a precipitating cloud top and lying in a radiometer's field of view represents the culmination of a complex interaction between emitted microwave radiation and its ongoing extinction through overlapping regions of liquid, melting phase, and ice. The encounter with the ice region represents the final interaction between the upwelling microwave radiation and the cloud constituents. Hence, an ice phase characterization perhaps represents a more inherently retrievable property from a combination of scattering-based channels above 37 GHz than the underlying rainfall. Model computations of top-of-atmospheric microwave brightness temperatures T_B from layers of precipitation-sized ice of variable bulk density and ice water content (IWC) are presented. The 85-GHz T_B is shown to depend essentially on the ice optical thickness, while the possibility of using the 37- and 85-GHz brightness temperature difference ΔT_B to estimate the integrated ice water path (IWP) is investigated. The results demonstrate the potential usefulness of using scattering-based channels to characterize the ice phase and suggest a top-down methodology for retrieval of cloud vertical structure and precipitation estimation from multifrequency passive microwave measurements.

Radiative transfer model results using the multiparameter radar data initialization from the Cooperative Huntsville Meteorological Experiment (COHMEX) in northern Alabama are also presented. The vertical behavior of the simulated multifrequency T_B, albedo, and extinction is presented along with the associated multiparameter radar measurements during the cloud lifecycle. Ice water path values estimated from the radar measurements are compared with the above theoretical computations for the corresponding T_B values and show agreement for values of IWP less than 1 kg m^{-2}. Above this, assumptions in the form of the ice-size distribution fail to adequately characterize the ice scattering process. Brightness temperature T_B warming effects due to the inclusion of a cloud liquid water profile are shown to be especially significant at 85 GHz during later stages of cloud evolution.

1. Introduction

The fundamental behavior of top-of-atmosphere (TOA) brightness temperatures at millimeter wavelengths is well known (Wu and Weinman 1984; Wilheit 1986; Spencer et al. 1989). Emission-based schemes function over oceans near operating frequencies of 19 GHz, where light to moderate precipitation rates cause a brightness temperature T_B increase over the radiometrically cold ocean surface. Scattering effects saturate the emission signal beyond a rain rate R of 20 mm h^{-1}. As the operating frequency increases, rapid increases of the volume scattering coefficient ultimately give rise to significant scattering of the cumulative upwelling radiation away from the radiometer field of view. Near 90 GHz, the single scattering coefficient for ice exceeds that of rain past a rain rate of about 10 mm h^{-1}, resulting in a cold TOA T_B. Unlike the emission-based method, the dynamic range of the scattering-based method is high (i.e., the slope of any theoretical T_B versus R curve is highly negative over a wide range of rain rates) when precipitation-sized ice particles are present and the underlying surface is essentially opaque past a few millimeters per hour.

Combinations of both emission- and scattering-based methods perhaps represent the best hope for passive spaceborne sensing of precipitation, independent of the underlying surface (Simpson et al. 1988). Essentially, the emission signal originates in the liquid and melting phase hydrometeors (lower altitudes, lower frequencies), while the scattering "signal" modulates the emission signal, mainly in regions of ice (higher altitudes, higher frequencies). Since TOA brightness temperatures represent a vertically integrated effect at the frequency of interest, the vertical structure of the hydrometeor phase and type and the associated size and shape distributions determine the intensity of the microwave emission and extinction. Recently, significant contributions to the understanding of the evolution of T_B behavior have resulted from coupling of either cloud model output or radar observations to microwave radiative transfer models. Smith and Mugnai (1988) and Mugnai and Smith (1988) examined the time evolution of the cloud-drop distribution in a time-dependent cloud model, noting the tendency for cloud

Corresponding author address: Dr. Vivekanandan, Dept. of Electrical Engineering, Colorado State University, Fort Collins, CO 80523.

liquid water to bias those theoretical T_B–R relations based on computations involving only precipitation-sized drops. Additionally, Mugnai et al. (1990) have developed two types of vertical weighting functions for each hydrometeor species using the Colorado State University RAMS (Regional Atmospheric Modeling System) model, which represent the vertical structure of the microwave thermal emission and its subsequent extinction for a given operating frequency. Adler et al. (1990) studied the evolution of T_B versus R relations throughout the time evolution of a 3D cloud model, also observing the tendency for coexisting ice and cloud liquid water to warm the TOA T_B. In addition, the T_B versus R relations were seen to evolve with time. Both results demonstrate the inadequacy of T_B versus R relations for precipitation retrieval that are based on a single frequency and a static storm vertical structure. Knowledge of a single TOA T_B over a cloud structure is not sufficient to reconstruct the cloud vertical structure uniquely; the situation is analogous to an underdetermined set of equations. Using a multifrequency statistical analysis, Kummerow et al. (1989) and Kummerow and Liberti (1990) varied the input parameters in a microwave radiative transfer model in such fashion as to impose agreement between the observed and model-derived multifrequency T_B and obtained significant concurrence between radar- and model-derived rain rates.

Cloud models provide detailed information regarding the particle-size distribution or mixing ratio of each cloud constituent throughout the model cloud as it evolves in time. When coupled with radiative transfer models, diverse sensitivity studies regarding the role of the vertical distribution of hydrometeor types upon the cumulative upwelling microwave radiation are available. Although concurrent radar and airborne radiometer data cannot be analyzed in such fine detail, and microphysical properties must be inferred indirectly from such radar observables such as reflectivity and differential reflectivity Z_{DR}, this arrangement does permit the joint analysis of the cloud structure as it physically exists during the flight duration. During the 1986 Cooperative Huntsville Meteorological Experiment (COHMEX), the first set of research-quality, coordinated multiparameter radar and airborne radiometer measurements were recorded (Williams et al. 1987). In an earlier publication by the authors (Vivekanandan et al. 1990b), microphysical inferences garnered from the NCAR CP-2 multiparameter radar during COHMEX were used in an attempt to eliminate many unrealistic storm vertical structures from the T_B inversion process in hopes of improving passive microwave precipitation estimation from space. Fulton and Heymsfield (1989) also compared coincident CP-2 scans and radiometer measurements from a series of airborne radiometer observations during COHMEX. Brightness temperature T_B evolution agreed qualitatively with the time–height evolution of the radar observables.

There has been a continuing interest in the utilization of multiparameter radar products as a remote sensing tool for cloud physics. Multiparameter radar observables are dependent upon the distributions of the particle size, shape, orientation, and composition throughout the radar pulse volume. Forward modeling studies of the behavior of differential reflectivity Z_{DR}, 3-cm specific attenuation A_3, and the linear depolarization ratio (LDR) were performed by Bringi et al. (1986) when studying graupel melting behavior and hail detection in Colorado storms. Recent modeling studies of the zero-lag cross correlation between the horizontally (H) and vertically (V) polarized returns ρ_{HV}, the associated differential phase shift ϕ_{DP}, and its range derivative K_{DP} have been carried out at 10-cm wavelength by Steinhorn and Zrnić (1988) and Balakrishnan and Zrnić (1989) in hopes of further characterization of rain and hail-size distributions and mixed-phase characterization. Vivekanandan et al. (1990a) used the Rasmussen and Heymsfield (1987) graupel–hail melting model to compute the vertical profiles of Z_{DR}, A_3, LDR, and K_{DP} at frequencies matching those of the NCAR CP-2 and German DLR polarimetric radars. Caylor and Illingworth (1989) and Illingworth and Caylor (1989) have interpreted S-band (3 GHz) LDR and ρ_{HV} measurements in the melting bright band and ice phases. Since oriented ice crystals can yield significant ϕ_{DP}, it is hoped that its implementation in radar processors will allow improved characterization of the ice phase throughout precipitating storms (Evans and Vivekanandan 1990).

Given the need for additional information regarding cloud vertical structure, the emphasis of a particular hydrometeor type on TOA T_B at several frequencies, and the inherent ambiguity of the T_B inversion process, the question remains, "What physical quantities can one meaningfully extract from a multifrequency combination of passive sensors within a tolerant degree of accuracy and certainty?" Rain rate, being at the bottom of the cloud vertical structure as observed by the downward-viewing sensors, can never be linked directly to any observed TOA T_B (although emission-based schemes over ocean surfaces approach this ideal). The overlying cloud structure always modulates the surface rain emission signal with varying degrees of emphasis depending on the frequency of observation.

Where present, however, the overlying ice remains relatively unobscured from the sensors, perhaps presenting an ice phase characterization as the most observable passive microwave measurement available with scattering-based microwave frequencies above 37 GHz and reinforces the notion of characterizing the cloud vertical structure from the top down. Few quantitative studies regarding the influence of ice-particle microphysics upon the upwelling microwave radiation

have been undertaken. Since the significance of passive microwave techniques toward improved global precipitation estimation has long been recognized and studied, nearly all theoretical studies have tended to link the underlying rain rate at the surface to the observed T_B. This is because early satelliteborne radiometers operated at or near emission-based frequencies where T_B warming could be explained in terms of rain rates over ocean computed from nearby radars. As the technology has advanced toward higher, scattering-based frequencies, relations linking T_B to an equivalent rain rate become ambiguous since the T_B depression arises mainly from regions of scattering located near and above the rain region. Hence, perhaps proper characterization of the upper ice region should be the initial step toward the eventual estimate of the underlying precipitation. Smith and Mugnai (1989) conclude that the major factor determining the higher-frequency TOA T_B is the vertical scale of the ice column and note the importance of the freezing mode (i.e., bulk ice density) at the highest frequencies. Vivekanandan et al. (1990b) questioned the assumption of a fixed bulk ice density for the ice distribution, observing TOA 92-GHz T_B differences of near 40 K due to a change in the bulk ice density from 0.6 to 0.9 g cm^{-3}. Using the Mueller matrix for small aspherical ice particles, Evans and Vivekanandan (1990) calculated the multiparameter radar products and the scattered Stokes vector. At 85 and 157 GHz, significant T_B polarization differences were noted depending on the bulk density, maximum particle size, and aspect ratio. Active microwave techniques of estimating precipitation and microphysics of storms have advanced considerably due to multifrequency and multipolarization techniques (Bringi et al. 1986; Bringi and Hendry 1990). But multifrequency passive techniques are yet to be exploited to their full extent for estimation of bulk cloud atmospheric properties other than rain rate.

In this study, we will explore the feasibility of retrieving the precipitation-sized integrated ice water path (IWP) from scattering-based T_B observations. Our approach will consist of simulations of the upwelling T_B from layered models containing ice layers characterized by different ice density and ice water contents. Although inherent uncertainty exists in a vertical structure reconstruction from purely passive microwave observations, it is hoped that estimates of the bulk amount of precipitation-sized ice will lend credence to the accompanying precipitation estimates.

2. Simulations of ice scattering effects to quantify ice water path

It is well known that an ice layer interacts with upwelling microwave emission essentially through a scattering process. The scattering increases with frequency, bulk density ρ, and the size of the ice particle (Heymsfield and Palmer 1986), imparting a drastic cooling in T_B for a given ice water content (IWC) and the associated vertically integrated ice water path (IWP), defined by

$$\mathrm{IWP} = \int_{Z_{\mathrm{bot}}}^{Z_{\mathrm{top}}} \mathrm{IWC}(z)dz, \qquad (1)$$

where the ice water content at a height z is defined by

$$\mathrm{IWC}(z) = \frac{4\pi}{3} \int_{r_{\mathrm{min}}}^{r_{\mathrm{max}}} \rho(z, r)r^3N(z, r)dr. \qquad (2)$$

The quantities r_{min} and r_{max} represent the radii of the minimum and maximum sizes in the ice particle size distribution $N(z, r)$; z_{bot} and z_{top} represent the bottom and top heights of the ice region; $\rho(z, r)$ is the ice density for a given height z and radius r. Radiative transfer models that include multiple scattering due to ice (Spencer et al. 1989; Smith and Mugnai 1989) characterize the ice layer only as solid ice spheres of bulk density ρ of 0.92 or 0.45 g cm^{-3}. In reality, precipitable ice can exist at varying bulk densities and contents depending on the environmental conditions. Thus, it is important to study the effects of ρ on the upwelling microwave radiation. Although the dielectric constant ϵ_r of an ice particle changes very little between 18 and 85 GHz for a given ice-particle bulk density, scattering due to the ice layer modulates the upwelling brightness temperature T_B in a nonlinear fashion. Mugnai et al. (1990) have described a "generalized weighting function" (GWF) that is indicative of "contributions due to radiation that originates both as emission and scattering and reaches the sensor without any further interaction with the atmospheric constituents." Such functions peak at higher altitudes for graupel at frequencies of 37 and 85 GHz over the main core of storms that contain significant ice quantities. Their studies suggest that it may be possible to use 37- and 85-GHz T_B measurements over precipitating clouds to retrieve some information on the ice phase alone. As mentioned in section 1, a brightness temperature represents the culmination of an integrated effect through the entire cloud structure. If the 37- and 85-GHz T_B are relatively independent of the intensity and depth of the underlying rain, perhaps these integrated-effect brightness temperatures are related in some fashion to the integrated ice water path. The following sections will describe a theoretical basis for the possible existence of such a relation.

a. Single-scattering characteristics of ice

For a given frequency, the volume scattering coefficient k_{sca} representing a polydispersion of ice particles increases with the bulk density of the ice particles. For a given integrated ice water path, it is possible to get a wide range of brightness temperature depressions due to scattering depending on the bulk density of the ice scatterers. To quantify the scattering due to ice at vary-

ing bulk densities, radiative transfer model results are presented for a variety of ice distributions characterized by different densities ρ and ice water contents.

Particle shapes are assumed to be spherical and Mie scattering techniques are used to obtain the scattering characteristics. Particles with a bulk density less than 0.9 g cm^{-3} are treated as an air–ice mixture, and the corresponding dielectric constant was computed as outlined in Tiuri et al. (1984). For exponential size distributions of varying ice content and bulk densities, total scattering cross sections are computed. All particles in the size distribution are assumed to exist with the same bulk density. Since the absorption is negligible in the absence of any water component, the albedo is nearly (but never exactly) unity.

To quantify the ice extinction coefficient for combinations of various bulk densities and ice water contents, a two-parameter analysis was performed. An exponential size distribution was assumed and the slope and intercept were varied to produce ice water contents up to 3.5 g m^{-3}. The upper limit of 3.5 g m^{-3} represents an equivalent meltwater rain rate of near 100 mm h^{-1}. Integration was carried out over radii ranging from 100 μm to 3 mm, independent of the density used. The following results were obtained at frequencies of 18, 37, and 85 GHz:

18 GHz:

$$k_{\text{ext}} = 0.012\rho^{0.286}\text{IWC}^{1.67} \tag{3}$$

37 GHz:

$$k_{\text{ext}} = 0.180\rho^{0.489}\text{IWC}^{1.60} \tag{4}$$

85 GHz:

$$k_{\text{ext}} = 2.08\rho^{0.701}\text{IWC}^{1.41} \quad \text{IWC}/\rho \leq 0.5$$

$$k_{\text{ext}} = 1.71\rho^{0.458}\text{IWC}^{1.19} \quad \text{IWC}/\rho \geq 0.5, \tag{5}$$

where k_{ext} is the extinction coefficient (km^{-1}) ρ is the bulk ice density (g cm^{-3}) and IWC is the ice water content (g m^{-3}), as defined in (2). The accuracy of the fit decreased with increasing frequency and k_{ext}, but in all cases the correlation coefficient between the actual and fitted values of k_{ext} exceeded 0.995.

These quantitative relations show that the extinction coefficient increases with frequency for the simple exponential, fixed-limits size distribution used. The bulk extinction coefficient increases roughly by a factor of 15 between 18 and 37 GHz, which can be explained by λ^4 scaling in wavelengths. The increase in extinction coefficient is reduced between 37 and 85 GHz, signifying that Mie scattering effects are significant. Scattering of upwelling microwave radiation depends on ice optical depth τ, which in turn depends on the ice k_{ext}. From the above equations, it can be deduced that optical depth τ at 85 GHz is roughly 150 times greater than that at 18 GHz. Hence, ice-layer scattering is significantly enhanced at 85 GHz compared to that at 18 GHz.

Mugnai et al. (1990) note that unlike the emission process, the scattering process is very sensitive to the ice-size distribution, which itself is variable with respect to height. Therefore, the form of Eqs. (3)–(5) may change significantly if the ice-size distribution deviates from an exponential form.

b. Dual-frequency technique to infer ice water path

Estimation of rain rate by passive microwave techniques is affected by the presence of other cloud constituents such as cloud liquid water, melting phases, and ice particles. Brightness temperature T_B warming effects due to melting were discussed in Vivekanandan et al. (1990b). Smith and Mugnai (1988) demonstrated the effects due to cloud water on rainfall rate estimates over oceans. Brightness temperature T_B depressions resulting from the presence of precipitation-sized ice has been shown by multilayer radiative transfer models and measurements over convective storms (Wu and Weinman 1984; Spencer et al. 1989)

In relation to ice-layer effects on upwelling radiation, only T_B depressions have been correlated with storm severity, such as the presence of hail (Fulton and Heymsfield 1989). Also, it is known that over land, in the absence of an ice layer, the variation in the 37- and 85-GHz TOA T_B is small (10–20 K) in comparison to T_B depressions that could otherwise be as high as 100 K with the ice layer. Beyond 10 mm h^{-1}, the upwelling T_B from a single layer of rain alone is not significantly affected by further increases in the rain intensity (Fig. 5, Vivekanandan et al. 1990b). Thus, in principle, microwave frequencies such as 37 and 85 GHz that are sensitive to scattering due to ice can be used to characterize the ice layer rather than the rain layer. The method outlined here is only a first attempt to quantify the ice layer and is simplified by eliminating other effects, such as the presence of cloud water and a melting phase. Of these two, the documented T_B "masking effect" due to the presence of coexisting cloud water and ice presents the most serious shortcoming to the practicality of this technique, as mentioned in section 1. We are currently investigating correction techniques to account for cloud-water contamination of T_B.

For this study the assumption of plane-parallel atmosphere is invoked. The vector radiative transfer model determines the Stokes parameters for radiation diffusely scattered, absorbed, and emitted by the atmosphere. The general method of solution for the radiative transfer problem is based on the method of doubling and adding (Stephens 1976). The essence of the method relies on the repeated use of the linear nature of the interaction principle, which itself is a statement of the interaction of radiation with the medium through the reflection and transmission matrices. The

radiative transfer model used in this section has two layers (ice overlying rain) and includes surface emission and reflection effects (Vivekanandan et al. 1990b). In general, the radiation transfer model can accommodate as many layers as needed depending on the inhomogeneity of the vertical storm structure. This feature will be utilized in section 3.

As the ice extinction coefficient k_{ext} was quantified in terms of ice density ρ and ice water content, we wish to quantify the T_B behavior over simulated clouds consisting of an ice layer overlying a rain layer. As before, the ice layer is also characterized by a bulk density ρ, ice water content, and in this case, thickness. Upwelling brightness temperatures were computed at 37 and 85 GHz using radiative transfer model computations at a 51° view angle for ice layers consisting of various combinations of ρ and IWC. The 51° view angle has been used by other researchers and lies between the incidence angles of the SMMR (49°) and SSM/I instruments (53°). In order to conserve mass between the rain and ice layers, the intercept coefficient of the exponential ice-size distribution (N_0^{ice}) was scaled to the rain exponential distribution such that $N_0^{ice}\rho^{ice} = N_0^{rain}\rho^{rain}$, where ρ^{ice} (denoted hereafter simply as ρ) varied from 0.2 to 0.9 g cm^{-3} throughout the simulations. Another way to conserve mass would be to scale the ice particle radii according to the ice density in some prescribed fashion while leaving $N_0^{rain} = N_0^{ice}$. As pointed out by Mugnai et al. (1990), the scattering process is very sensitive to the distribution of the ice particle sizes, unlike the emission process. For each simulation, the ice-layer optical depth τ at 85 GHz and the vertically integrated ice water path IWP were also calculated for graphical display.

Figure 1a shows TOA 85-GHz T_B versus the ice optical thickness τ for 4-km ice layer overlying a 4-km rain layer, the ice layer possessing a range of ice bulk densities as labeled. Obviously, many of the points at either end of the curves represent physically unlikely situations. For example, high-density ice such as hail is most likely found in thunderstorms with high values of ice water content. Conversely, low-density ice such as snowflakes is often found in winter storms with low amounts of ice water content. Eliminating these, the ice τ only varies by about 25% for a given T_B above 100 K. Figure 1b shows the TOA 37–85 GHz T_B difference (hereafter denoted by ΔT_B) versus the vertically integrated ice water path (IWP) for the same simulations as in Fig. 1a. In the absence of any ice, the curves show an inherent 10–20 K ΔT_B due to differing emissive and scattering effects from the underlying rain alone, which rises to near 100 K when larger ice water contents and ice densities are introduced. Past an IWP > 3 kg m^{-2} and $\rho > 0.4$ g cm^{-3}, ΔT_B begins to decrease. This is due to the near balance between emission and scattering in the rain layer at 85 GHz. As a result, the emission emanating from the top of the rain layer remains fairly constant, and the TOA 85-GHz T_B "bottoms out" past a given rain rate. At 37 GHz, a similar effect occurs at a reduced intensity, so the TOA 37-GHz T_B still decreases. Therefore, the 37–85 GHz T_B difference begins to decrease from its peak value. Below this IWP threshold the ΔT_B–IWP curves nearly merge together independent of the ice density, which is in the range of physically realizable situations in heavy thunderstorms. In addition, computations using other ice-layer thicknesses superimpose upon Figs. 1a,b closely. This is not too surprising, since IWP and τ both rep-

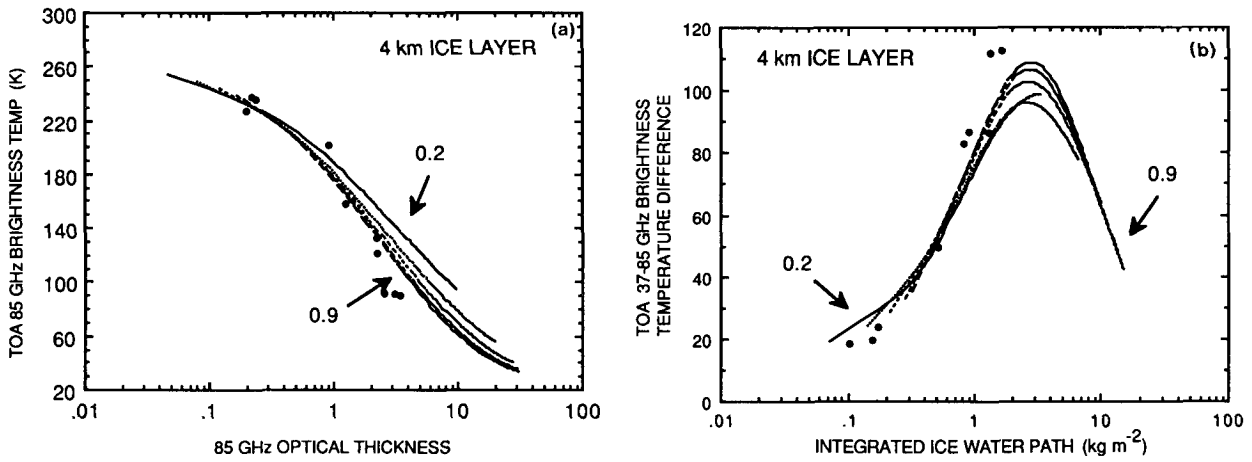

FIG. 1. (a) 85-GHz TOA T_B vs ice optical thickness τ and (b) TOA 37–85 GHz T_B difference ΔT_B vs vertically integrated ice water path (IWP) for a 4-km ice layer overlying a 4-km rain layer. Each curve represents a different ice density, where the ice density ranges from 0.2 to 0.9 g cm^{-3}. The points on each curve represent rain rates from 0 to 100 mm h^{-1}. The intercept N_0 of the exponential ice-size distribution has been scaled to conserve mass throughout both layers. Discrete data points represent results from the COHMEX modeling presented in section 3.

resent a vertically integrated effect; values of which can result from various combinations of ρ, ice water content, and layer thickness, in much the same way that T_B also represents an integrated effect due in part to these same constituents.

Such dual-frequency schemes have been utilized in the past. Before the 85 GHz capability of radiometers such as that aboard the SSM/I were available, Spencer and Santek (1985) used the 18–37 GHz T_B difference from *Nimbus-7* SMMR observations to map the extent of global convection over land. The differencing scheme was adopted to remove many effects due to variations underlying the rain region, such as surface emissivity and thermal temperature, since this T_B difference is much less affected by these variations than is single-channel data. At 37 and 85 GHz, the sensitivity to surface emissivity variations is reduced (Mugnai et al. 1990), especially over regions containing significant ice. Similarly, the 37–85 GHz T_B difference is also less affected by the effects underlying the ice region, such as the vertical extent and intensity of the rain region, which is the major source of the upwelling radiation that the ice scatters. Model results show that the variation in both the 37- and 85-GHz TOA T_B due to variations in rain-layer thickness and intensity is about 20–30 K over a land surface characterized by an emissivity of 0.9. Differencing the two T_B removes much of this variation. Hence, this T_B differencing scheme removes much of the variation that may exist in regions below the ice, allowing ice characterizations to take place that may otherwise be more ambiguous when interpreted from a single channel. We have not performed simulations containing an ocean surface. Since a calm ocean is both radiometrically cold and highly polarized, lower frequency channels such as 19 GHz can be used to identify this situation. Also, the emissivity of a calm ocean surface increases with frequency, thereby yielding negative values of ΔT_B. This technique for IWP retrieval is analogous to the use of near-infrared (NIR) and infrared (IR) T_B differences for remotely sensing the optical thickness of cirrus clouds, based on the fact that particle albedo decreases with increasing particle radius in the NIR, while albedo increases with increasing particle radius in the more strongly absorbed IR region (Stone et al. 1990).

Figure 2a shows TOA 85-GHz T_B versus ice optical thickness τ for a 0.4 g cm^{-3} ice layer overlying a 4-km rain layer and a range of ice-layer thicknesses as labeled. Again, many of the points at either end of the curves represent physically unlikely situations, and the ice τ varies slightly more for a given T_B than in Fig. 1a. The corresponding ΔT_B–IWP curves in Fig. 2b also show somewhat more deviations from each other than in Fig. 1b, but when some situations are eliminated (i.e., the region of decreasing ΔT_B as explained earlier) the curves still demonstrate considerable dynamic range (about 50 K ΔT_B over an order of magnitude in IWP). Computations performed at other average bulk densities show similar features in regard to the behavior of Figs. 2a,b.

3. Detailed microwave radiative transfer modeling of a COHMEX storm

The 20 July 1986 storm from the COHMEX experiment in northern Alabama has been studied extensively through the use of both multiparameter radar observations and cloud modeling (Tuttle et al. 1989; Wakimoto and Bringi 1988). The storm was observed by three Doppler radars, including the CP-2 multiparameter radar operated by NCAR. Cloud tops reached 14 km, and the resultant collapse produced hail, heavy

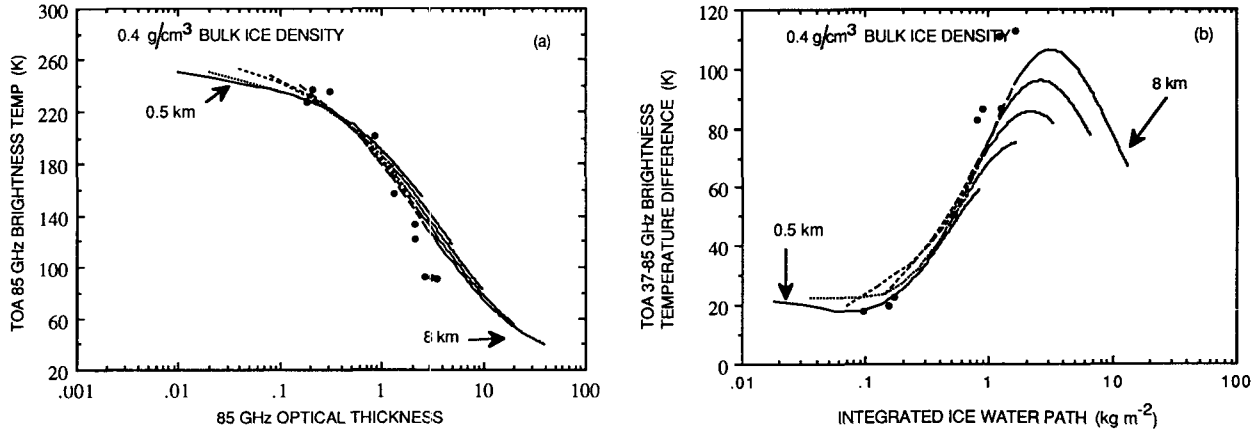

FIG. 2. 85-GHz TOA T_B vs ice optical thickness τ and (b) TOA 37–85 GHz T_B difference ΔT_B vs vertically integrated ice water path (IWP) for 0.4 g cm^{-3} bulk ice density layer overlying a 4-km rain layer. Each curve represents an ice-layer thickness, ranging from 0.5 to 8 km. The points on each curve represent rain rates from 0 to 100 mm h^{-1}. The intercept N_0 of the ice-size distribution has been scaled to conserve mass throughout both layers. Discrete data points represent results from the COHMEX modeling presented in section 3.

rain, and a 30 m s^{-1} differential radial velocity microburst. The life cycle of the main activity from growth to collapse was approximately 30 min. Details of the synoptic conditions along with coincident cloud photography and CP-4 scans are given in Wakimoto and Bringi (1988), while a detailed discussion of the storm microphysical evolution in relation to the multiparameter radar observables is presented by Tuttle et al. (1989). The latter reference also presents output of a two-dimensional, time-dependent cloud model.

Based on the vigorous microphysical conditions that accompanied the 20 July storm, we feel that this storm represents an excellent candidate for microwave radiative transfer modeling. Current research efforts in this area are directed toward multifrequency observations and improved characterization of vertical bulk microphysical structure (Kummerow et al. 1989). In an earlier study by the authors (Vivekanandan et al. 1990b), multiparameter radar data gathered with the CP-2 radar during the 23 June 1986 storm was used to initialize a microwave radiative transfer model. Results were compared with a series of ER-2 overflights gathering TOA radiometer measurements at 18, 37, and 92 GHz. The model was limited to three layers, and only radar data in the vicinity of the brightness temperature minimum was used. Since the ER-2 navigation can drift 3–4 km h^{-1} (Galliano and Platt 1990), difficulties were encountered in aligning the brightness temperature time series with the corresponding features in the radar data.

Recent improvements in the radiative transfer model incorporate a multiparameter radar "module" to directly compute the extinction coefficient, albedo, and Mie phase matrices from the various radar products coefficient. The input radar data are stored in MUDRAS format (Mohr and Miller 1983). For the CP-2 radar, this input data includes both horizontal and vertically polarized 10-cm reflectivities (Z_H and Z_V, respectively), 3-cm LDR, and 3-cm horizontally polarized reflectivity X_H corrected for attenuation using the method of Tuttle and Rinehart (1983), all in units of decibels (dB). From these products, one can obtain the 3-cm specific attenuation A_3 in units of decibels per kilometer (dB km^{-1}), the differential reflectivity $Z_{DR} = Z_H - Z_V$, and the attenuation-corrected dual-frequency ratio (DFR $= Z_H - X_H$). The vertical spacing chosen during the MUDRAS processing determines the layer thickness of the plane parallel radiative transfer model. In this study, we have used $\Delta x = \Delta y = 0.25$ km and $\Delta z = 0.5$ km. The radiative transfer model described in section 2b was refined for this application. The up- and downwelling Stokes vector in between each 0.5-km thickness layer is available to allow for direct comparison of the vertical evolution of the upwelling brightness temperatures, extinction, and albedo alongside the vertical profile of the radar observables over the horizontal region of interest. Although only the top of atmosphere (TOA) radiances are recorded by spaceborne or airborne radiometers, behavior of the cumulative upwelling brightness temperatures, extinction coefficients, and albedo is useful for studying the role that the bulk particle microphysics in modulating the upwelling radiances. This is especially useful in studying the effects of the melting process, addition of cloud liquid water, and bulk ice density variations.

a. Incorporation of the CP-2 data into the model

The CP-2 volume scans were interpolated into a three-dimensional array of points with the radar at the Cartesian origin. The layered model incorporates three stages of water phase: rain, melting (water-coated ice spheres), and ice. The two parameters of the rain exponential size distribution $N(D) = N_0 \exp(-\Lambda D)$ were computed as detailed in Vivekanandan et al. (1990b). These were computed for every Δz thickness up to 2.4 km above ground, where the melting process is assumed complete or nearly so. Briefly, this method uses the Z_H and Z_{DR} measurements averaged at each height over the horizontal region of interest (denoted by $\bar{Z}_H$ and $\bar{Z}_{DR}$) as the dependent variables in a rain-rate relationship. Above this, the intercept N_0 of the exponential size distribution for the melting and ice layers is scaled as to follow the observed $\bar{Z}_H$ reflectivity profile up to the 10-dBZ cloud top. A linear decrease in the volume fraction of meltwater on melting ice spheres is assumed up to the level of the disappearance of the 3-cm specific attenuation $\bar{A}_3$. All particles in the distribution of the melting phase contain the same volume fraction of water. The limits of integration for the size distribution ranged from 100-μm to 3-mm radius, independent of density. As discussed, the choice of a suitable bulk ice density plays a major role in determining the scattering coefficient of the ice-particle size distribution and hence the amount of scattering taking place in the upper ice layers. We have used a value of 0.9 g cm^{-3} in the presence of any dual-frequency ratio hail signal, and 0.6 g cm^{-3} elsewhere. The H and V surface emissivity can be specified at each quadrature angle; for this study we used an unpolarized Lambertian surface with an emissivity of 0.9. A vertical temperature profile of 6.5°C km^{-1} is taken into account for thermal emission and dielectric constant ϵ_r. Surface temperature was set to 25°C.

b. Effects of nonprecipitating cloud water

One provision that must be accounted for heuristically is the presence of nonprecipitating cloud water. Radars operating at wavelengths of 3–10 cm are not sensitive to normal amounts of cloud water. Since the cloud water drops are small (<100 μm) compared with the wavelengths of both the radar and radiometer fre-

quencies, the absorption (and hence extinction) coefficient of cloud water is independent of the cloud drop-size distribution and is given by (Gossard and Strauch 1983):

$$k_{\text{ext}}^{\text{cloud}} = (0.434)\frac{6\pi}{\rho\lambda}\,\text{Im}(-K)M_{\text{cloud}}\ (\text{dB km}^{-1}); \quad (1)$$

where M_{cloud} is the cloud liquid water content (LWC, g m^{-3}), λ the wavelength (cm), ρ the density (g cm^{-3}), and Im$(-K)$ is the imaginary part of $(-K)$, where $K = (\epsilon_r - 1)/(\epsilon_r + 2)$; Im$(-K)$ increases quickly below $\lambda = 1$ cm and also increases with decreasing water temperature. At 10 GHz, a 1 g m^{-3} cloud LWC at 0°C gives rise to about 0.1 dB km^{-1} of extinction, below the accuracy in which we can currently estimate the specific attenuation A_3 using attenuation-correction techniques.

Cloud-water effects can be significant at all commonly used radiometer frequencies. Near 19 GHz, TOA T_B increases over a cool ocean represent contributions from the lower altitude liquid phase, but high cloud LWCs from nonprecipitating clouds can also produce T_B warming over a radiometrically cold ocean surface. The extinction due to a 1 g m^{-3} cloud LWC at 85 GHz and a temperature of −10°C is considerable (about 5 dB km^{-1} or 1 km^{-1}). Since supercooled cloud LWC does not contribute significantly to scattering, its net effect when coexisting with ice is to increase the overall extinction and hence reduce albedo, thereby reducing the scattering "signal" where present and warming the TOA T_B. This "masking effect" was noted by Smith and Mugnai (1988) and Adler et al. (1990), especially at later cloud development times and higher frequencies, where deep ice layers have formed in the presence of supercooled cloud water existing at temperatures below −10°C. Due to the nearly invisible nature of cloud water as far as radar detection is concerned, we will test the effect of introducing a prescribed profile of cloud water in the next section.

c. *Time evolution of the storm microwave radiative transfer*

A thorough explanation of the 20 July 1986 storm evolution using the CP-2 radar observables is given in Tuttle et al. (1989); we will quote their results often. From 1340 to 1405 CDT (all times will refer to central daylight time), small cells with 7-km maximum cloud tops exhibited 45-dBZ maximum reflectivity with Z_{DR} values as high as 3 dB. Caylor and Illingworth (1987) noted similar values in Great Britain and suggested that these positive Z_{DR} columns were indicative of a small concentration of large supercooled raindrops ascending in an updraft. Lack of any significant specific attenuation A_3 indicates small amounts of precipitation-sized LWC.

The vertical profile of the horizontally averaged CP-2 radar products $\bar{Z}_H$, $\bar{Z}_{\text{DR}}$, and $\bar{A}_3$ over the cloud dimensions at 1406 is shown in Fig. 3a. Differential reflectivity $\bar{Z}_{\text{DR}}$ is obtained by taking the ratio of $\bar{Z}_H$ and $\bar{Z}_V$ over the region of interest. Near 7-km height, $\bar{Z}_{\text{DR}}$ values have fallen to near 0 dB while $\bar{A}_3$ retains values of about 0.8 dB km^{-1}, suggesting the increased presence of cloud and smaller precipitation-sized drops. A strong updraft of 25 m s^{-1} is present (Tuttle et al. 1989). The peak $\bar{Z}_H$ is elevated to near 5-km height, where larger-sized supercooled raindrops are present.

The vertical profile of the model 18-, 37-, and 85-GHz upwelling T_B is shown in Fig. 3c. Effects of cloud LWC inclusion are shown on dashed curves. Unless otherwise stated, the superimposed cloud LWC vertical profile started at cloud base (1.5 km), reached 1 g m^{-3} at −10°C (5.4 km), and tapered back to zero near −35°C (9.4 km). This may be realistic during the early stages of cloud growth by collision–coalescence processes; nevertheless, we have retained it throughout for comparative purposes. From Fig. 3c, 85-GHz cloud LWC effects become significant near 5.5-km height and contribute to a 7-K TOA warming from 227 to 234 K. Figure 3d shows that the 85-GHz albedo (albedo denoted by ω) is affected by cloud LWC above 2.5 km, falling from 0.5 to 0.4. At 37 and 85 GHz, ω quickly rises to near 1.0 above 8 km, where glaciation is starting to occur, and emission due to atmospheric water content is reduced. An abrupt discontinuity in ω occurs at all frequencies, near the region of glaciation.

At all three frequencies, the T_B vertical gradient decreases sharply near the 4-km height. At 85 GHz, T_B steadily decreases with height above 0.5 km; similar behavior at 18 GHz is not noted until near 3 km. This behavior is borne out in the vertical profile of extinction coefficient k_{ext} shown in Fig. 3b. The 85-GHz k_{ext} exceeds 1.2 km^{-1} near the surface, resulting in a rapid increase in the associated optical thickness τ. For all frequencies, k_{ext} peaks near the $\bar{Z}_H$ maximum.

At 1409, initial appearance of the DFR hail signal was noted near 7-km height, indicative of continued growth by accretion and freezing (Fig. 4). The DFR values are between 3 and 4 dB. The attenuation $\bar{A}_3$ has increased to 1.2 dB km^{-1}, reaching a maximum near the hail signal (liquid to ice) region. The vertical extent of positive $\bar{Z}_{\text{DR}}$ was reduced, with the $\bar{Z}_H$ peak collocated with near zero $\bar{Z}_{\text{DR}}$. At 1412, the region of DFR hail signal extended to 8.5 km. Surface rainfall had increased, and the large $\bar{A}_3$ core near 5 km began to descend.

At 1414, cloud tops reached 13 km, and the updraft had weakened. The CP-2 RHIs show a distinct Z_{DR} "notch" located near the surface, indicating that hail was now reaching the surface (Bringi et al. 1986). The reflectivity $\bar{Z}_H$ consists of two distinct maximums, the upper one collocated with a strong region of DFR hail signal and the lower one immediately below the peak

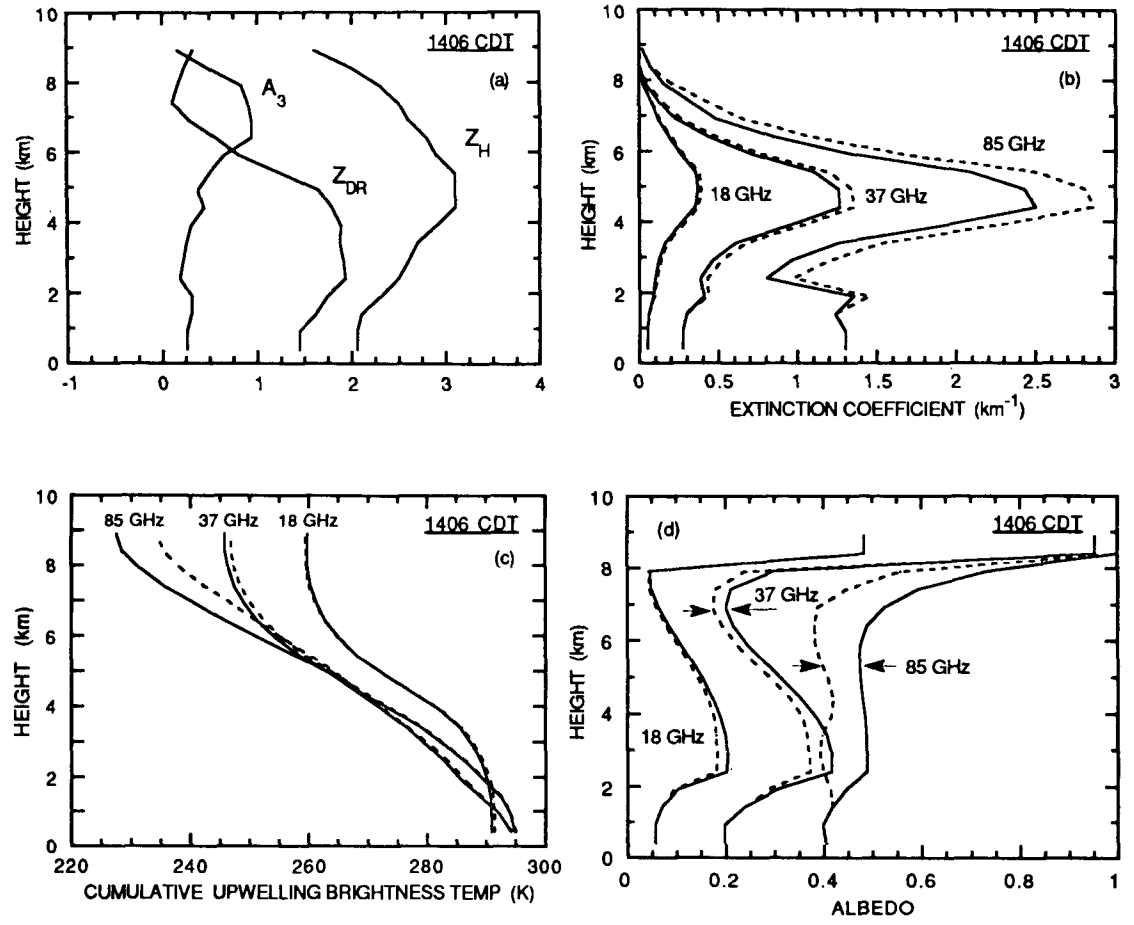

FIG. 3. Radiative behavior at 18, 37, and 85 GHz at 1406 CDT 20 July 1986. (a) Vertical profile of the horizontally averaged radar products $\bar{Z}_H$ (scaled by a factor of 0.1), $\bar{Z}_{DR}$, and $\bar{A}_3$; (b) vertical profile of the associated cloud extinction coefficient; (c) vertical profile of the simulated cumulative upwelling T_B based on CP-2 multiparameter radar-initialized radiative transfer modeling; and (d) vertical profile of the associated cloud albedo. Adjacent dotted-line curves include a cloud liquid water profile as discussed in section 3.

$\bar{A}_3$ of 1.5 dB km^{-1} (Fig. 5a). DFR values reached their peak of 5–8 dB here. This enhancement in $\bar{A}_3$ falls below the region of DFR hail signal, where the initial melting of the ice gives rise to an $\bar{A}_3$ enhancement (Hansman 1986; Vivekanandan et al. 1990a). Brightness temperature T_B behavior is illustrated in Fig. 5c. The 37- and 85-GHz T_B fall to 210 to 110 K, respectively, with cloud LWC responsible for 8 and 20 K of TOA T_B warming, respectively. Cloud LWC effects become noticeable above 3 km. The 18-GHz T_B behavior remains relatively unaffected above 4.5 km, while 85 GHz falls steadily in the upper and lower regions of melting and ice, respectively. Interestingly, the upwelling 37-GHz T_B exhibits two distinct peaks in its vertical gradient, near 4 and 8 km. Evidently, the cumulative upwelling radiance is influenced by the extinctive properties of the LWC near 4 km, as well as the scattering properties of the hail aloft. The 37-GHz

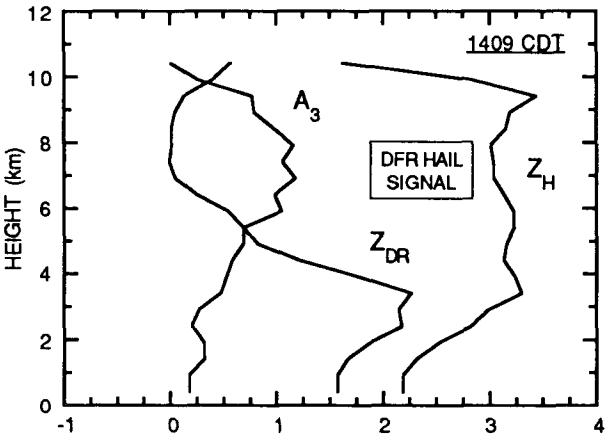

FIG. 4. Vertical profile of the horizontally averaged CP-2 radar products at 1409 CDT 20 July 1986; $\bar{Z}_H$ is scaled by a factor of 0.1.

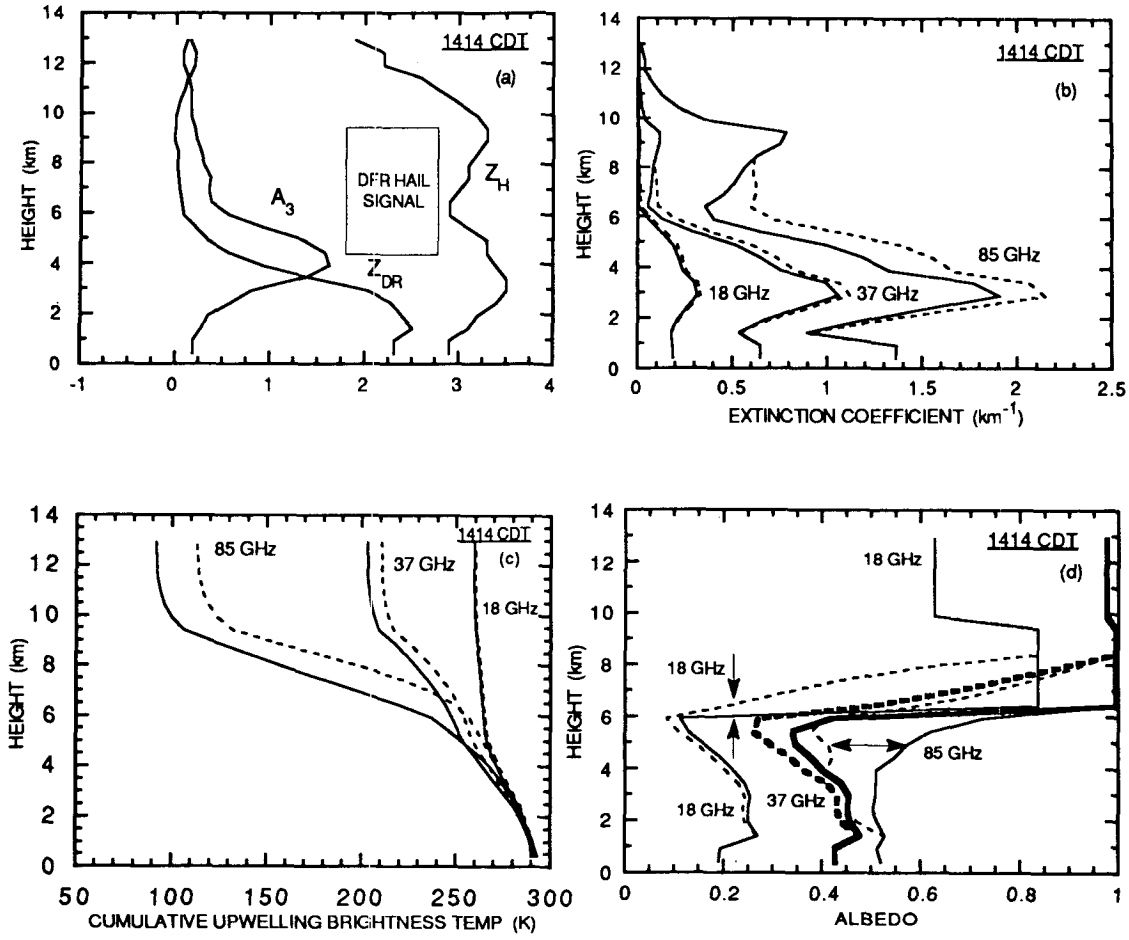

FIG. 5. Same as Fig. 3, except at 1414 CDT. The 37-GHz albedo profile is shown in bold lines.

k_{ext} reaches only 0.1 dB km^{-1} near 8–10 km in Fig. 5b, due to ice scattering ($\omega \approx 0.98$), while $\omega \approx 0.4$ near 4 km (Fig. 5d), indicating extinction is nearly split between absorption and scattering of the melting hail and rain. The 85-GHz k_{ext} magnifies this effect; it reaches a peak k_{ext} of 2.2 and 0.8 km^{-1} near 3 and 9 km, respectively. The ice scattering and enhanced absorption effect due to melting is strong enough at 85 GHz to produce a steady vertical gradient in the associated T_B over the entire region of the DFR hail signal.

The vertical profiles of $\bar{Z}_H$, $\bar{Z}_{DR}$, and $\bar{A}_3$ at 1420 is shown in Fig. 6. During this time the precipitation core continued its descent to the ground. The average rainfall $\bar{R}$ of 35 mm h^{-1} reached its peak at 1420, where the $\bar{A}_3$ core had nearly reached the surface, reaching a peak value of 1.5 dB km^{-1} near 3 km. The $\bar{Z}_{DR}$ column has collapsed, increasing near the freezing level and reaching a peak of 2.1 dB at the surface. A smaller, lower region of DFR hail signal is present and the double maximum in $\bar{Z}_H$ is still noticeable.

Near 1423, the DFR hail signal disappeared and the reflectivity core had nearly reached the surface, as shown in Fig. 7a. The attenuation $\bar{A}_3$ increases steadily

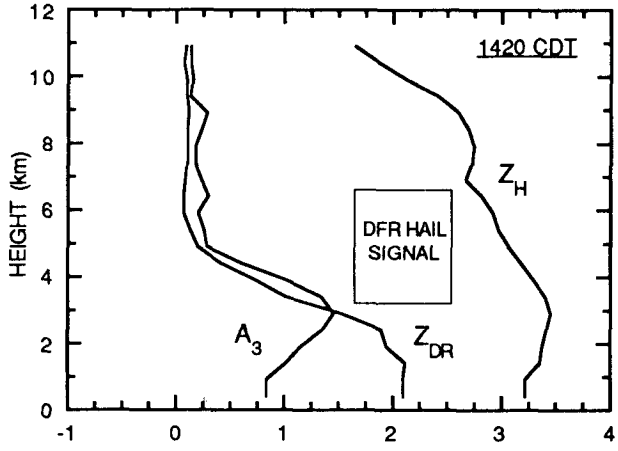

FIG. 6. Vertical profile of the horizontally averaged CP-2 radar products at 1420 CDT during 20 July 1986; $\bar{Z}_H$ is scaled by a factor of 0.1.

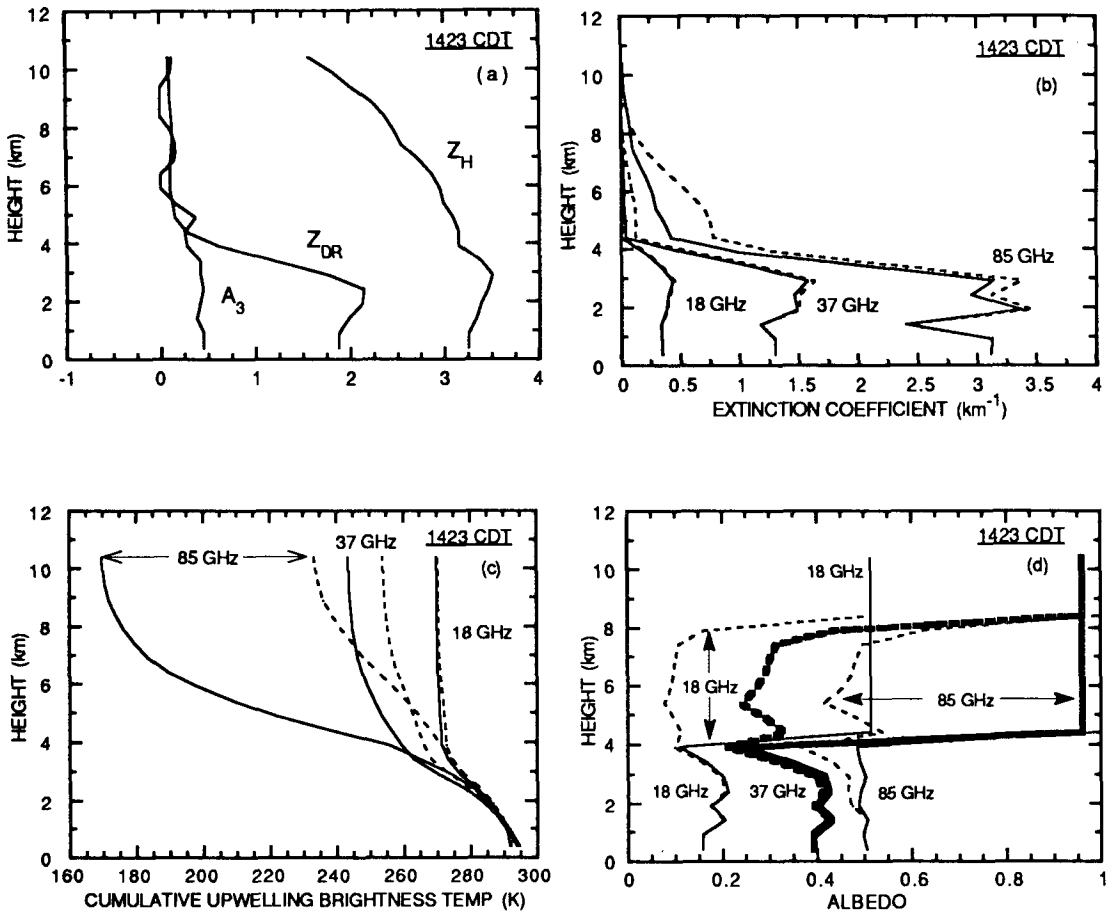

FIG. 7. Same as Fig. 3, except at 1423 CDT. The 37-GHz albedo profile is shown in bold lines.

downward, reaching a peak of only 0.5 dB km^{-1} near the surface. Cloud tops were near 11 km and $\bar{Z}_{DR}$ increased steadily below the freezing level of 4.5 km with a slight depression near the surface indicative of rain mixed with small hail. Both the 37- and 85-GHz TOA T_B have warmed since 1420. Large values of $\bar{Z}_H$ and $\bar{Z}_{DR}$ near 3 km yield extreme values of k_{ext}, reaching 3.5 km^{-1} at 85 GHz (Fig. 7b). As noted in Figs. 7b,d, cloud LWC effects change the vertical profiles of k_{ext} and ω significantly above the freezing level of near 4.5 km. Brightness temperature T_B behavior is affected by cloud LWC somewhat lower, near 3 km, where there is already some effect on the reduction of the 85-GHz albedo and its associated T_B warming. As before, 18-GHz upwelling T_B remains essentially unaffected by an addition of cloud LWC.

Note that if cloud LWC is not included in the 1423 model, the lack of any significant precipitation-sized liquid or melting hydrometeors among the ice above 4.5 km produces a sharp discontinuity in the vertical profile of ω, regardless of frequency, as seen in Fig. 7d. Smith and Mugnai (1989) have also noted this when considering the effects of large ice particles in a precipitating model cloud, the absence of a mixed phase thereby "misrepresenting the layers which would, under normal conditions, contain a mixture of water and ice particles." While our superimposed cloud LWC profile somewhat filters out this discontinuity, it also greatly warms the upwelling 85-GHz T_B from 170 to 233 K. Brightness temperature T_B warming due to cloud LWC quickly reaches 55 K by 6 km. With cloud LWC, the 85-GHz ω remains near 0.5 up to 8 km, destroying much of the scattering effects of the precipitation-sized ice particles by adding additional emission. The 18- and 37-GHz albedos are similarly affected, but reach a TOA value of only 0.52 and 0.96, respectively. The reduction in 37-GHz ω is enough to produce a 10 K warming in TOA T_B, while 18-GHz k_{ext} near 6 km is so slight that any redistribution of scattering–emission effects are not discernible throughout the T_B vertical profile. These vertically detailed radiative transfer model computations demonstrate the sensitivity of the cumulative upwelling T_B to the dynamic microphysical structure of the storm.

A complete time history of the simulated TOA T_B and average rain rate $\bar{R}$ derived from radar as described earlier is shown in Fig. 8. With the onset of the DFR hail signal in the radar data, 85-GHz T_B falls rapidly, bottoming out near 90 K from 1414–1420, while $\bar{R}$ increases from 15 to 35 mm h^{-1}. Effects of cloud LWC increase 85-GHz TOA T_B from 113 to 182 K over the same time interval. Although the superimposed cloud LWC profile is not realistic at later cloud times, it does demonstrate that cloud water significantly affects any rain-rate retrieval schemes that may use the 37- and 85-GHz channels. The 37-GHz T_B behavior smoothly decreases, then increases over the 30-min period, reaching a minimum T_B of 202 K near 1414. The TOA response at 18 GHz, being mainly sensitive to the amount of underlying liquid water content, shows nice agreement with trend of the vertically integrated meltwater path (MWP) (plotted in Fig. 9), with limited T_B dynamic range over the warm land surface. The integrated meltwater path is computed by replacing IWP and IWC with MWP and liquid water content (LWC), respectively, in Eqs. (1) and (2), and replacing the density $\rho(z,r)$ with the constant value of 1 g cm^{-3}. Until 1409, the collision–coalescence vertical growth of the storm produced an increase in MWP from 5 on to 7.5 kg m^{-2}, while the 18-GHz T_B cooled from 275 to 250 K. From 1409 to 1414, the MWP fell to 5.5 kg m^{-2} (due to glaciation), while the 18 GHz T_B rose only 10 K, due to the limited dynamic range of the 18-GHz channel over land surfaces (Vivekanandan et al. 1990b). The 3-K cooling is noted at 1417 when the MWP rises back to near 8 kg m^{-2} (due to increased rainfall and melting hail).

In contrast, the noncloud water contaminated 85-GHz TOA T_B follows the associated ice optical thickness, as illustrated in Fig. 10, suggesting, along with Figs. 1a and 2a, that the TOA 85-GHz T_B is essentially dependent upon the optical thickness of the ice water path. Especially at later cloud times, the "masking effect" of the cloud water is evident. Referring back to Figs. 1a and 2a, the discrete data points plotted in these figures represent the noncloud water contaminated T_B values resulting from this radar study, and follow the theoretical curve nicely for 85-GHz $T_B > 140$ K. Values of T_B noted beyond these represent physical situations that our oversimplified two-layer model of rain and ice failed to classify. In part, this is due to our choice of a fixed, bulk density independent of size and the fixed limits used for integrating over the ice size distribution independent of the ice density ρ. The 37–85 GHz T_B difference, ΔT_B behavior is plotted in Fig. 11. Without the effects of cloud LWC, ΔT_B follows the integrated ice water path (IWP) trend, but the addition

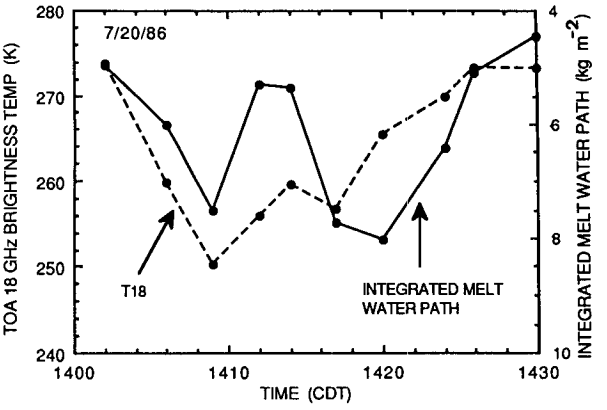

FIG. 9. Time evolution of the vertically integrated meltwater path (MWP, kg m^{-2}) (including a cloud-water profile) and the model computed TOA 18-GHz T_B from 20 July 1986.

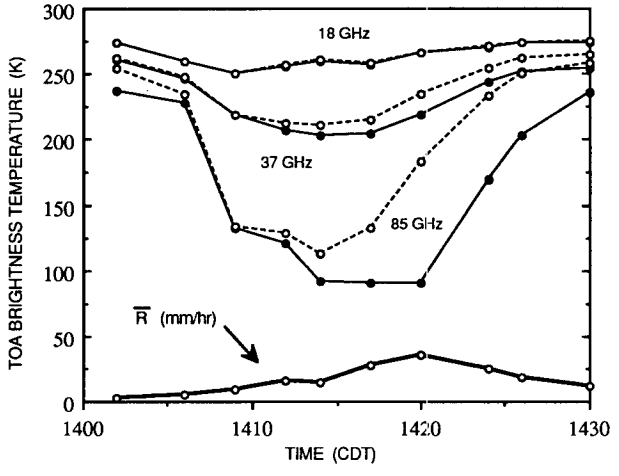

FIG. 8. Time evolution of the simulated TOA T_B at 18, 37, and 85 GHz during 20 July 1986. Dashed lines represent inclusion of a cloud liquid water profile. The heavy solid line represents the CP-2 radar-derived average rain rate $\bar{R}$ at 1.4-km height.

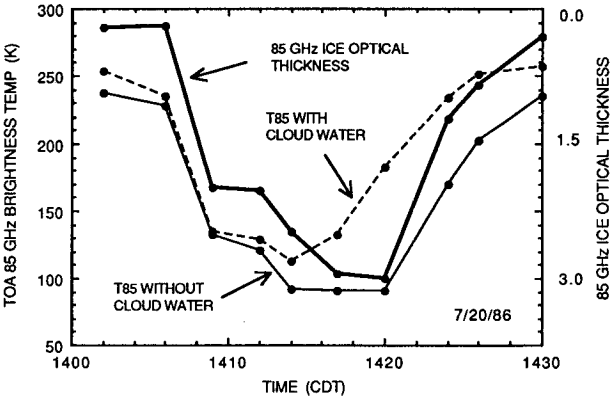

FIG. 10. Time evolution of the 85-GHz ice optical thickness τ and the model computed TOA 85-GHz T_B from 20 July 1986, showing the T_B effects resulting from inclusion and exclusion of a cloud liquid water profile.

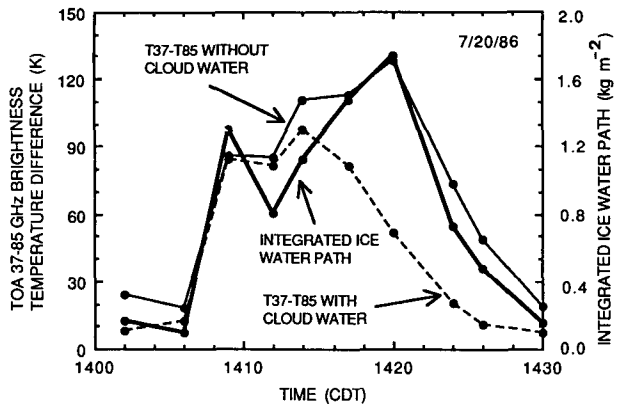

FIG. 11. Time evolution of the vertically integrated ice water path (IWP, kg m^{-2}) and the model computed TOA 37–85 GHz T_B difference ΔT_B for 20 July 1986, showing the T_B effects resulting from inclusion and exclusion of a cloud liquid water profile.

of cloud LWC reduces ΔT_B, distorting the ΔT_B–IWP relationship, especially during periods where the DFR hail signal is present. Referring back to Figs. 1b and 2b, the data points overlaid on these figures represent the noncloud water ΔT_B values resulting from the radar modeling and agree quite well with the theoretical ΔT_B–IWP curves below 100 K or 2 kg m^{-2}. Again, our theoretical modeling cannot account for ΔT_B values above this, which correspond to a deep ice layer not well characterized by our assumption of an exponential distribution with fixed integration limits and ice density independent of size.

4. Conclusions

The variation in the scattering characteristics from ice hydrometeors are discussed with regard to the ice bulk density ρ at multiple microwave frequencies. It is shown that for a given vertically integrated ice water path (IWP) and bulk ice density ρ, the ice optical depth τ at 85 GHz is roughly 150 times that at 18 GHz, suggesting the possible usefulness of 85- and 37-GHz TOA T_B observations for ice water path characterization. In the absence of an ice layer, the 37- and 85-GHz TOA T_B emanating from the rain layer remain essentially unchanged as rain rate increases. Additionally, upwelling radiation at 37 and 85 GHz through an ice layer differs due to differential scattering characteristics, unlike the rain layer, which retains an albedo below 0.5 even at 85 GHz. Thus, these frequencies are suitable to infer vertically integrated ice properties such as the ice water path. Unlike the rain region, the ice layer remains relatively unobscured from a spaceborne radiometer, perhaps presenting an ice-phase characterization as a more inherently retrievable property than the rain (liquid) phase.

A simple two-layer radiative transfer model utilizing a variable thickness ice layer at various bulk densities, ice water contents, and underlying rain rates is studied with regard to variation in TOA T_B. It is demonstrated that the TOA 85-GHz T_B is essentially dependent upon the ice optical depth τ to produce steep cooling in T_B. In terms of a physical (we mean nonelectromagnetic) property of a precipitating cloud, it has been shown that the 37–85 GHz T_B difference ΔT_B can possibly be used to estimate the physcial property of integrated ice water path. These model results represent only a simple first attempt to demonstrate that the inherent scattering properties associated with an ice layer can be successfully used to quantify the ice layer regardless of surface emissivity and underlying rain variations. Several limitations currently exist with this technique. Over convective cores, both the 37- and 85-GHz weighting functions may peak higher into the ice region due to stronger scattering by the largest ice particles, thereby underestimating the total ice water path (Yeh et al. 1990). A simple ice exponential size distribution with bulk ice density independent of size, and fixed limits of integration independent of the ice content present does not well characterize many ice habits, but appeared to function adequately for ice water contents below 1 g m^{-3}. Since the scattering process is very dependent upon the form of the assumed ice-size distribution, these assumptions are worthy of further investigation. It is worth noting that the compact nature of the curves in Figs. 1 and 2 results only when the view angles are identical; differing 37- and 85-GHz view angles destroy this ΔT_B behavior. This made tests with the COHMEX airborne radiometer datasets difficult, since these radiometers scan and view differently. Even though downward-viewing radiometers measure only the TOA microwave T_B, which represents an integrated effect due to all layers, this oversimplified model does demonstrate that the differential frequency scattering characteristics resulting from ice potentially represent a means to infer quantitative information on the upper vertical structure of storms. This information can then be fed back into a vertical structure model and additional lower-frequency T_B observations, eventually resulting in a rain rate estimate that is both physically and radiatively consistent with the microphysical conditions above it. This methodology of characterizing the upper layers first with the highest frequencies and then working downward toward the rain region incorporates microphysical information more inherently contained in a collection of TOA T_B at various operating frequencies with successively lower altitude bulk microphysical characterizations. We are currently further investigating this methodology.

Detailed microwave radiative transfer modeling of a strong convective storm from 20 July during the COHMEX experiment was presented. Single-scattering properties of each 0.5-km-thick layer were estimated from CP-2 multiparameter radar measurements for

subsequent input into a radiative transfer model. Effects due to nonprecipitating cloud water are also considered in model computations. During the early stages of cloud evolution, the absence of significant glaciation caused the T_B to be dominated by emission, since the corresponding albedo ω was less than 0.5 for most of the vertical structure of the storm. Thus, the T_B masking effect due to cloud water is negligible. Around 1414, a strong DFR hail signal (signifying a ice density closer to 0.9 g cm^{-3}) and a significant ice-layer thickness both combine to sharply reduce the cumulative 37- and 85-GHz T_B throughout the region of DFR hail signal. Above 6 km, ω rises sharply, and coexistence of cloud water and significant ice content reduce the effective ω and the resultant 85-GHz T_B warming is noticeable. As the storm reduces in intensity in terms of IWP near 1423 and the DFR hail signal disappears, TOA T_B warming effects due to cloud water are most significant, as the presence of cloud water between 4 and 8 km drastically reduces ω. However, much of the warming effect is due to our use of a time-independent cloud LWC profile, which inserts unrealistic quantities and vertical profiles of cloud LWC at later cloud times, where the precipitation has taken on a stratiform nature. These detailed vertical profiles of extinction and albedo, and the resultant cumulative upwelling T_B at various frequencies and significantly different microphysical conditions, present a physical explanation for much of the TOA T_B behavior.

Because the 18-GHz T_B has a poor dynamic range over the rain rates observed, and since both the 37- and 85-GHz T_B are modulated by the ice layer, CP-2 radar-derived average rain rates compare poorly with any single TOA T_B. However, ΔT_B values seemed to compare well with the theoretical curves presented in Figs. 1b and 2b for small to moderate values of IWP. Beyond IWP $>$ 1 kg m^{-2} and 85-GHz $\tau > 2$, the theoretical curves overestimated when compared with the CP-2 radar-derived quantities. Much of the difference is due to our vertical scaling of the ice-size distribution intercept N_0^{ice} as to match the decreasing reflectivity (Z_H) profile, as well as our choice of fixed limits of integration for the ice-size distribution, and ice density ρ independent of size. The 18-GHz TOA T_B depressions do correlate well with higher values of the vertically integrated meltwater path (MWP), but are severely restricted by a lack of sensitivity to higher MWP ($>$5 kg m^{-2}). This should be overcome when sensing over a low emissivity ocean surface due to the resulting increase in the dynamic range of the 18-GHz emission signal. Unfortunately, the presence of cloud water currently introduces a shortcoming toward a practical application of these passive dual-frequency techniques for a characterization of the full vertical IWP. Recent investigations at CSU using coupled radiative transfer and cloud model output has shown that it is still possible to estimate the portion of the vertical IWP that lies above the region of most supercooled cloud water. By comparing cloud-water–free radiative transfer model results with actual passive T_B observations, it may be possible to estimate the vertical extent of the supercooled cloud water by purely passive techniques. In short, the presence of cloud water need not be a impenetrable barrier to estimation of the ice phase in precipitating clouds. We are currently investigating multiple frequency methods to account for the ice scattering masking effect resulting from coexisting ice and cloud liquid water, as well as effects resulting from variations in the form of the assumed ice-size distribution.

The model computations are shown only for a single convective storm for which well-documented multiparameter radar data are available. The methodology presented here could be tested in practice if suitable radar and radiometer data can be gathered in addition to cloud microphysics information such as ice-layer thickness and ice water content, such as was planned for the Advanced Microwave Precipitation Radiometer (AMPR) instruments during the future Convection and Precipitation Experiment (CaPE) in Florida. In addition, the techniques described here may be extendable to winter storms, provided that the storm is intense enough to significantly scatter upwelling radiation from the surface.

Acknowledgments. Two of the authors (JV and VNB) acknowledge support from NASA Grant NAG8-643. J. Turk is a fellow of the Army Research Office's Center for Geosciences at Colorado State University. The authors wish to thank Dr. Graeme L. Stephens of Colorado State's Atmospheric Sciences Department for his advice and assistance. Radiative transfer computations were performed on the Cray supercomputers at the National Center for Atmospheric Research in Boulder, Colorado, and the Center for Computer Assisted Engineering (CCAE) at Colorado State University.

REFERENCES

Adler, R. F., N. Prasad, H.-Y. M. Yeh, W. Tao and J. Simpson, 1990: The effect of convective life cycle stage on microwave brightness temperature–rainrate relations as determined from 3-D cloud model results. *Seventh Conf. on Atmospheric Radiation,* San Fransisco, Amer. Meteor. Soc., J64–J71.

Balakrishnan, N., and D. S. Zrnić, 1989: Use of cross-correlation between orthogonally polarized echoes to characterize precipitation and infer hail size. *J. Atmos. Sci.,* **47,** 565–583.

Bringi, V. N., and A. Hendry, 1990: Technology of polarization diversity radars for meteorology. *Radar in Meteorology,* D. Atlas, Ed., Amer. Meteor. Soc. 153–190.

——, R. M. Rasmussen and J. Vivekanandan, 1986: Multiparameter radar studies in Colorado convective storms. Part 1: Graupel melting studies. *J. Atmos. Sci.,* **43,** 2545–2563.

Caylor, I. J., and A. J. Illingworth, 1987: Radar observations and modeling of warm rain initiation. *Quart. J. Roy. Meteor.,* **113,** 1171–1191.

——, and ——, 1989: Identification of the bright band and hydrometeors using co-polar dual polarization radar. *24th Amer. Meteor. Soc. Conf. Radar Meteorology,* Tallahassee, Amer. Meteor. Soc., 9–12.

Evans, K. F., and J. Vivekanandan, 1990: Multiparameter radar and microwave radiative transfer modeling of nonspherical atmospheric ice particles. *IEEE Trans. Geosci. Remote Sens.,* **28,** 423–437.

Fulton, R., and G. M. Heymsfield, 1989: Multiparameter radar and passive microwave radiometric comparisons of convection during COHMEX. *24th Conf. on Radar Meteorology,* Tallahassee, Amer. Meteor. Soc., 304–308.

Galliano, J. A., and R. H. Platt, 1990: Advanced microwave precipitation radiometer (AMPR) for remote observation of precipitation. Tech. Rep. prepared for NASA George C. Marshall Space Flight Center, Available from. MSFC, AL, 35812.

Gossard, E. E., and R. G. Strauch, 1983: *Radar Observations of Clear Air and Clouds.* Elsevier, 280 pp.

Hansman, R. J., 1986: Microwave absorption measurements of melting spherical and nonspherical hydrometeors. *J. Atmos. Sci.,* **43,** 1643–1649.

Heymsfield, A. J., and A. Palmer, 1986: Relationships for deriving thunderstorm anvil ice mass for CCOPE storm water budget estimates. *J. Climate Appl. Meteor.,* **25,** 691–702.

Illingworth, A. J., and I. J. Caylor, 1989: Cross polar observations of the bright band. *24th Conf. on Radar Meteorology,* Tallahassee, Amer. Meteor. Soc., 323–327.

Kummerow, C. D., and G. L. Liberti, 1990: Precipitating cloud vertical structure derived from passive microwave radiometry. *Seventh Conf. on Atmos. Radiation,* San Fransisco, Amer. Meteor. Soc., J72–J80.

——, R. A. Mack and I. M. Hakkarinen, 1989: A self-consistency approach to improve microwave rainfall rate estimation from space. *J. Appl. Meteor.,* **28,** 869–884.

Mohr, C. G., and L. J. Miller, 1983: CEDRIC—a software package for Cartesian space editing, synthesis, and display of radar files under interactive control. *Proc. 21st Conf. on Radar Meteorology,* Edmonton, Amer. Meteor. Soc., 569–574.

Mugnai, A., and E. A. Smith, 1988: Radiative transfer to space through a precipitating cloud at multiple microwave frequencies. Part I: Model description. *J. Appl. Meteor.,* **27,** 1055–1073.

——, H. J. Cooper, E. A. Smith and G. J. Tripoli, 1990: Simulation of microwave brightness temperatures of an evolving hailstorm at SSM/I frequencies. *Bull. Amer. Meteor. Soc.,* **71,** 2–13.

Rasmussen, R. M., and A. J. Heymsfield, 1987: Melting and shedding of graupel and hail. Part 1: Model physics. *J. Atmos. Sci.,* **44,** 2754–2763.

Simpson, J., R. F. Adler and G. North, 1988: A proposed Tropical Rainfall Measuring Mission (TRMM) satellite. *Bull. Amer. Meteor. Soc.,* **69,** 278–295.

Smith, E. A., and A. Mugnai, 1988: Radiative transfer to space through a precipitating cloud at multiple microwave frequencies. Part 2: Results and analysis. *J. Appl. Meteor.,* **27,** 1074–1091.

——, and ——, 1989: Radiative transfer to space through a precipitating cloud at multiple microwave frequencies. Part 3: Influence of large ice particles. *J. Meteor. Soc. Japan.,* **67,** 739–754.

Spencer, R. W., and D. A. Santek, 1985: Measuring the global distribution of intense convection over land with passive microwave radiometry. *J. Climate Appl. Meteor.,* **24,** 860–864.

——, H. M. Goodman and R. E. Hood, 1989: Precipitation retrieval over land and ocean with the SSM/I. Part I: Identification and characteristics of the scattering signal. *J. Atmos. Oceanic Technol.,* **6,** 254–273.

Steinhorn, I., and D. S. Zrnić, 1988: Potential uses of the differential propagation phase constant to estimate raindrop and hailstone size distributions. *IEEE Trans. Geosci. Remote Sens.,* **26,** 639–648.

Stephens, G. L., 1976: The transfer of radiation through vertically nonuniform stratocumulus water clouds. *Contrib. Atmos. Phys.,* **49,** 237–253.

Stone, R. S., G. L. Stephens, C. M. R. Platt and S. Banks, 1990: The remote sensing of thin cirrus cloud using satellites, lidar, and radiative transfer theory. *J. Appl. Meteor.,* **29,** 353–366.

Tiuri, M., A. H. Sihvola, E. G. Nyfors, and M. T. Hallikaiken, 1984: The complex dielectric constant of snow at microwave frequencies. *IEEE J. Oceanic Eng.,* **OE-9,** 377–382.

Tuttle, J. D., and R. E. Rinehart, 1983: Attenuation correction in dual-wavelength analyses. *J. Climate Appl. Meteor.,* **22,** 1914–1921.

——, V. N. Bringi, H. D. Orville and F. J. Kopp, 1989: Multiparameter radar study of a microburst: Comparison with model results. *J. Atmos. Sci.,* **46,** 601–620.

Vivekanandan, J., V. N. Bringi and R. Raghavan, 1990a: Multiparameter radar modeling and observations of melting ice. *J. Atmos. Sci.,* **47,** 549–564.

——, J. Turk, G. L. Stephens and V. N. Bringi, 1990b: Microwave radiative transfer studies using combined multiparameter radar and radiometer measurements during COHMEX. *J. Appl. Meteor.,* **29,** 561–585.

Wakimoto, R. M., and V. N. Bringi, 1988: Dual-polarization observations of microbursts associated with intense convection: The 20 July storm during the MIST project. *Mon. Wea. Rev.,* **116,** 1521–1539.

Wilheit, T., 1986: Some comments on passive microwave measurement of rain. *Bull. Amer. Meteor. Sci.,* **67,** 1226–1232.

Williams, S. F., H. M. Goodman, K. R. Knupp and J. E. Arnold, 1987: SPACE/COHMEX Data Inventory Document, NASA Tech. Memo 4006.

Wu, R., and J. A. Weinman, 1984: Microwave radiances from precipitating clouds containing aspherical ice, combined phase, and liquid hydrometeors. *J. Geophys. Res.,* **89,** 7170–7178.

Yeh, H.-Y. M., N. Prasad, R. A. Mack and R. F. Adler, 1990: Aircraft microwave observations and simulations of deep convection from 18 to 183 GHz. Part II: Model results. *J. Atmos. Oceanic Technol.,* **7,** 392–410.